J. Fluid Mech. (2014), *vol.* 758, *pp.* 786–808. © Cambridge University Press 2014
doi:10.1017/jfm.2014.500

Freezing colloidal suspensions: periodic ice lenses and compaction

Anthony M. Anderson[1,†] **and M. Grae Worster**[1]

[1]Department of Applied Mathematics & Theoretical Physics, University of Cambridge, Wilberforce Road, Cambridge CB3 0WA, UK

(Received 14 January 2014; revised 9 August 2014; accepted 25 August 2014; first published online 14 October 2014)

Recent directional solidification experiments with aqueous suspensions of alumina particles (Anderson & Worster, *Langmuir*, vol. 28 (48), 2012, pp. 16512–16523) motivate a model for freezing colloidal suspensions that builds upon a theoretical framework developed by Rempel *et al.* (*J. Fluid Mech.*, vol. 498, 2004, pp. 227–244) in the context of freezing soils. Ice segregates from the suspension at slow freezing rates into discrete horizontal layers of particle-free ice, known as ice lenses. A portion of the particles is trapped between ice lenses, while the remainder are pushed ahead, forming a layer of fully compacted particles separated from the bulk suspension by a sharp compaction front. By dynamically modelling the compaction front, the growth kinetics of the ice lenses are fully coupled to the viscous flow through the evolving compacted layer. We examine the periodic states that develop at fixed freezing rates in a constant, uniform temperature gradient, and compare the results against experimental observations. Congruent with the experiments, three periodic regimes are identified. At low freezing rates, a regular periodic sequence of ice lenses is obtained; predictions for the compacted layer thickness and ice-lens characteristics as a function of freezing rate are consistent with experiments. At intermediate freezing rates, multiple modes of periodic ice lenses occur with a significantly diminished compacted layer. When the cohesion between the compacted particles is sufficiently strong, a sequence of mode-doubling bifurcations lead to chaos, which may explain the disordered ice lenses observed experimentally. Finally, beyond a critical freezing rate, the regime for sustained ice-lens growth breaks down. This breakdown is consistent with the emergence of a distinct regime of ice segregation found experimentally, which exhibits a periodic, banded structure that is qualitatively distinct from ice lenses.

Key words: phase change, solidification/melting, suspensions

1. Introduction

The freezing of colloidal suspensions is a process with both technological and environmental implications. By studying the freezing behaviour in colloid suspensions, we can begin to understand freezing phenomena in more complex heterogeneous systems (foams, gels, emulsions, tissues, etc.). A particularly important observation in these systems is that they do not freeze uniformly: the frozen phase (e.g. ice) becomes

†Email address for correspondence: a.anderson@damtp.cam.ac.uk

https://doi.org/10.1017/jfm.2014.500 Published online by Cambridge University Press

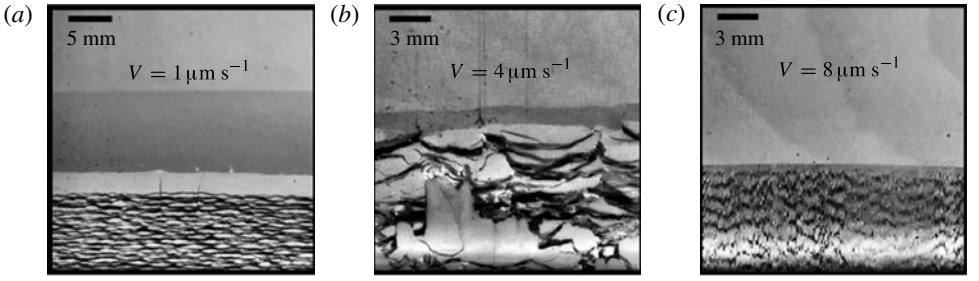


FIGURE 1. Images of ice segregation patterns from directional solidification experiments with colloidal alumina varying only the freezing rate (Anderson & Worster 2012). Freezing occurs from below, with segregated ice appearing black and particle-laden suspensions in shades of grey; the bulk suspension appears in the top portion of each image. The three regimes are shown: (*a*) periodic ice lenses with compacted layer (dark grey) and partially frozen layer (light grey); (*b*) disordered ice lenses with diminished compacted layer; (*c*) periodic ice banding, with no ice lenses or compacted layer, but evidence in the ice morphology of horizontal corrugations.

segregated, trapping bulk regions of colloid within. A rich set of ice segregation patterns are generated depending on the freezing conditions and suspension properties (Taber 1929; Deville *et al.* 2006, 2009; Peppin, Elliott & Worster 2006). In a process known as 'ice-templating', this phenomenon is utilized in the fabrication of bio-inspired porous materials and composites (Zhang *et al.* 2005; Deville *et al.* 2006). Other technological applications include cryobiology (Rapatz, Menz & Luyet 1966; Mazur 1984) and food engineering (Velez-Ruiz & Rahman 2007). In nature, ice segregation underlies frost heave, whereby saturated soils swell as they freeze (Taber 1929, 1930), which reshapes landscapes and inflicts costly damage to man-made structures (French 2007). A major goal in understanding all of these systems is to elucidate the physical processes by which ice becomes segregated in order to predict the conditions under which various patterns occur.

Anderson & Worster (2012) (hereafter AW) conducted freezing experiments with concentrated colloidal dispersions using a directional solidification apparatus to independently control the freezing rate and temperature gradient. The apparatus is similar to that used in alloy solidification (e.g. Peppin, Huppert & Worster 2008*a*) and in other studies of freezing suspensions (Watanabe & Mizoguchi 2000; Watanabe 2002; Peppin, Wettlaufer & Worster 2008*b*). In a series of experiments examining the quasi-steady behaviour at incremental freezing rates, AW observed two distinct types of periodic, banded ice segregation (figure 1). At the lowest freezing rates, the segregation pattern resembles ice lenses found in freezing soils (Taber 1929, 1930). At the highest freezing rates, alternating bands of particles and ice appear again with features that are qualitatively distinct from ice lenses. In particular, the particle-rich bands in this second regime exhibit additional ice segregation at a much finer scale than the bandwidth, which AW suggest are vertically oriented (dendritic) ice crystals, relating the ice-banding phenomena to what was observed in earlier experiments from Deville *et al.* (2009). These two regimes of ice segregation are separated by a third regime at intermediate freezing rates that features a highly disordered pattern of ice lenses.

Besides the pattern of ice segregation, another distinguishing feature between these three regimes appears in the structure of the suspension above the zone of

https://doi.org/10.1017/jfm.2014.500 Published online by Cambridge University Press

ice segregation. At the lowest freezing rates, there is an abrupt transition from the bulk suspension to a fully compacted layer (dark grey). At the compaction front, a stress-induced sol–gel transition occurs (Tsapis *et al.* 2005; Goehring, Clegg & Routh 2010), where compressive stresses from cyrostatic suction cause the dispersed particles from the bulk suspension to aggregate into a cohesive particle matrix. AW also identified a partially frozen layer (light grey) between the compaction front and the warmest ice lens and provide evidence to suggest that ice in this layer is present in the pore space of the particle matrix, forming a frozen fringe. As the freezing rate is increased, the regime of disordered ice lenses exhibits a substantially diminished compacted layer. At the highest freezing rates, the compacted layer is completely absent. These observations suggest that the compacted layer plays an essential role in controlling the freezing behaviour. The primary objective of this article is to elucidate the role of compaction in ice segregation.

To model the ice segregation and compaction, we adopt a theoretical framework developed by Rempel, Wettlaufer & Worster (2004) in the context of frost heave, whereby a new ice lens is initiated within a frozen fringe, which consists of pore ice that is connected directly to the preceding ice lens and extends up the temperature gradient through the porous matrix. The theory is related to 'rigid-ice' models for frost heave (O'Neill & Miller 1985; Fowler 1989) and uses force-equilibrium constraints to derive expressions for the ice-lens growth rates and nucleation conditions; however, in the formulation used by Rempel *et al.* (2004), the forces are derived directly from the thermo-physical interactions between the constituents of the partially frozen suspension. Our model extends the force-equilibrium constraints to allow for an evolving compaction front, where particles aggregate and form a cohesive matrix.

A full description of the problem is presented in § 2, including details about the compaction and aggregation of the suspension as well as details about the frozen fringe used in the mathematical formulation. In § 3, we summarize the theory developed by Rempel *et al.* (2004), adapting it where necessary to include the compacted layer. This leads to a one-dimensional model for the vertical structure of the freezing suspension, consisting of two coupled ordinary differential equations (ODE) for the position of the active ice lens and compaction front alongside algebraic conditions for the initiation of new ice lenses. In § 4 we analyse the model, focusing on periodic states in a constant, uniform temperature gradient at fixed freezing rates. The regime of periodic ice lenses at slow freezing rates is analysed in detail and compared directly to the experimental observations of AW. At higher rates of freezing, we show that the diminishing compacted layer eventually leads to a breakdown of the ice lensing and that the nature of the approach to breakdown is sensitive to the cohesive strength of the compacted layer. Finally, in § 5, we draw all of the predictions together and discuss their relevance to the experimental observations.

2. Problem description

2.1. *Directional solidification*

Consider an initially homogeneous colloidal dispersion with particle concentration ϕ_0 undergoing directional solidification, with the sample pulled at speed V through a constant, uniform temperature gradient G. This configuration, shown schematically in figure 2, conforms with experiments performed by AW and others (Watanabe & Mizoguchi 2000; Watanabe 2002; Peppin *et al.* 2008*b*). In these experiments, a constant temperature gradient is achieved by sandwiching a Hele-Shaw cell, containing the suspension, between two heat exchangers. In contrast to freezing from

https://doi.org/10.1017/jfm.2014.500 Published online by Cambridge University Press

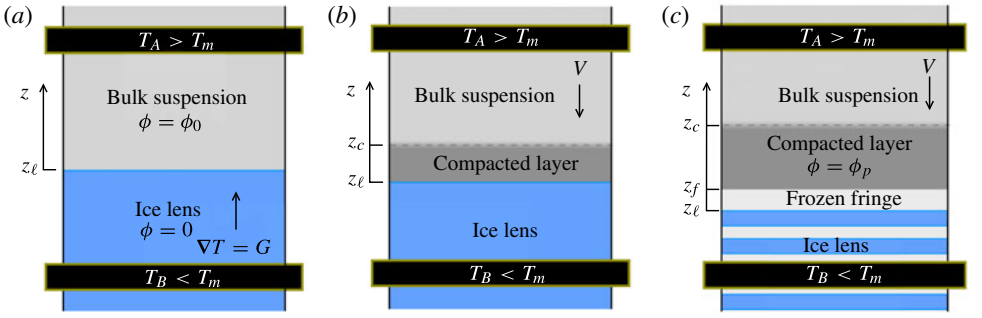


FIGURE 2. (Colour online) Directional solidification. The sample is pulled at speed V through a fixed temperature gradient G maintained by two heat exchangers, A and B, where $T_B < T_m < T_A$. (*a*) Initially, $V = 0$ and a single ice lens is in thermodynamic equilibrium with the bulk suspension. (*b*) When $V > 0$, there is an extended transient phase where particles build up ahead of the ice lens, forming a close-packed particle layer. (*c*) A frozen fringe forms in the late stages of unsteady growth, spawning a sequence of discrete ice lenses; after this transient phase, ice lenses form in a regular periodic sequence and the compacted layer reaches its maximum thickness.

a cold boundary held at a fixed temperature ('fixed chill'), directional solidification allows independent control of the freezing rate and temperature gradient. Consequently, a steady mean state is established for fixed V and G after a transient growth phase. The theoretical analysis that follows is primarily focused on prediction of the steady state.

The stages leading to periodic ice lenses are illustrated in figure 2. Initially, the sample is held stationary ($V = 0$) in a uniform temperature gradient with a single ice lens in thermodynamic equilibrium with the bulk suspension (figure 2*a*). Once the sample is put in motion, the ice lens begins growing to keep pace with the advancing isotherms. For sufficiently small pulling speeds ($V \lesssim 1$ μm s^{-1}), the ice lens rejects all of the particles from the bulk suspension, which in turn build up as a compacted layer (figure 2*b*). The ice lens retreats to colder temperatures as particles accumulate and impart added resistance on the flow of water feeding ice growth. At these colder temperatures, water in the pore space adjacent to the ice lens is cooled below the bulk melting temperature; once sufficient undercooling is attained, ice enters the pore space to form a frozen fringe. Under conditions described in detail below, a new ice lens is nucleated within the frozen fringe, intercepting the water supply of its predecessor, whose growth then ceases. This process repeats several times, eventually producing a regular periodic sequence of ice lenses (figure 2*c*).

2.2. *The compacted layer*

AW provide two key experimental observations about the compacted layer. The first observation is an abrupt change in particle concentration at the leading edge of the compacted layer. Recent theoretical work (Peppin *et al.* 2006, 2011) develops a theory for freezing suspensions that models the suspension as a hard-sphere colloidal (HSC) dispersion and predicts the formation of a sharp compaction front at the leading edge of a uniformly close-packed layer under conditions of limited Brownian diffusion. The length scale for Brownian diffusion is $\ell_D = D_0/V$, where D_0 is the Stokes–Einstein diffusivity. For the suspensions used by AW, it was estimated that

https://doi.org/10.1017/jfm.2014.500 Published online by Cambridge University Press

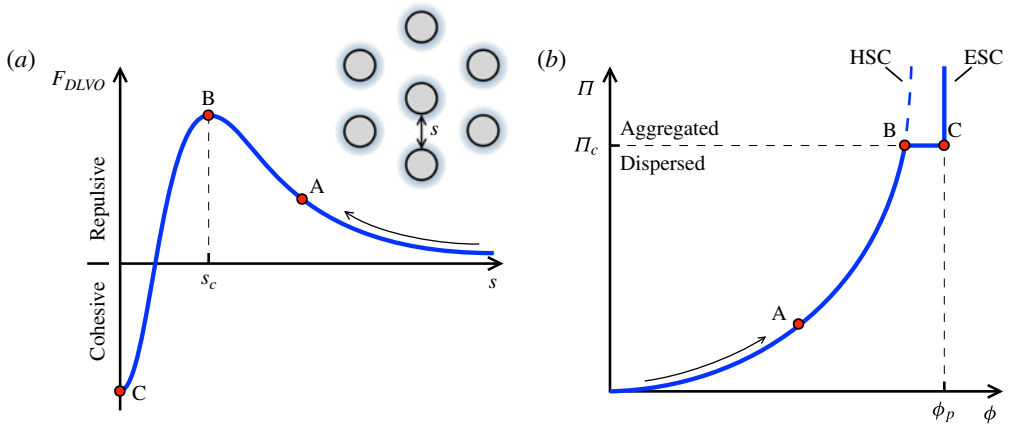


FIGURE 3. (Colour online) Compression of an electrostatically stabilized colloidal (ESC) dispersion. (*a*) The combination of electrostatic repulsion and van der Waals attractions produce an interparticle force F_{DLVO} (e.g. computed from a DLVO pair potential) which depends on the distance s separating particles. Down to a critical separation distance s_c, corresponding to the maximum repulsive force, macroscopic consolidation requires a compressive particle stress Π, (*b*). Due to the finite nature of the interparticle repulsions, ESCs undergo a stress-induced sol–gel transition (B $\rightarrow$ C) at a critical aggregation pressure Π_c. As long as compressive stresses remain below Π_c (e.g. A), the consolidation is reversible and the particles behave like hard-sphere colloids (HSCs); however, once $\Pi > \Pi_c$, the particles are bound by van der Waals attractions as a cohesive matrix. This latter transition is irreversible, such that if Π falls below Π_c, the cohesive strength of the matrix maintains the packing fraction $\phi = 0.64$.

$\ell_D \sim 1$ μm, indicating that diffusion is negligible. We ignore diffusion in our analysis and treat the boundary between the bulk suspension and the compacted layer as a sharp front with a jump in particle concentration. The compacted layer is assumed to be randomly close-packed, with particle fraction $\phi_p \approx 0.64$.

AW also observed that the compaction front is the site of a stress-induced sol–gel transition, where the dispersed particles irreversibly aggregate to form a cohesive matrix. The cryostatic suction produced by segregated ice growth exerts large compressive stresses that bring the particles into contact, causing aggregation. In an HSC model, particles are cohesionless, so that when freezing ceases and the compressive stresses are relieved, the close-packed particles disperse back into the bulk suspension. The HSC model is an idealization; in reality, particles in aqueous suspensions interact through a combination of van der Waals attractions and electrostatic repulsions, where Derjaguin–Landau–Verwey–Overbeek (DLVO) theory provides a prototypical model (Israelachvili 2011). The forces involved at various stages of consolidation of an electrostatically stabilized colloidal (ESC) dispersion are shown by the sequence A–B–C in figure 3. Cryostatic suction exerts a compressive stress Π on the particles, which respond through an adjustment of the mean particle spacing; the equilibrium particle concentration ϕ occurs where the net interparticle repulsions balance Π (e.g. point A). In DLVO theory, the competition between van der Waals and electrostatic forces results in a maximum repulsive force at a critical particle separation s_c, corresponding to a critical compressive stress Π_c (point B). Particles aggregate when $\Pi > \Pi_c$, at which point they are bound together by attractive van der Waals forces (point C).

https://doi.org/10.1017/jfm.2014.500 Published online by Cambridge University Press

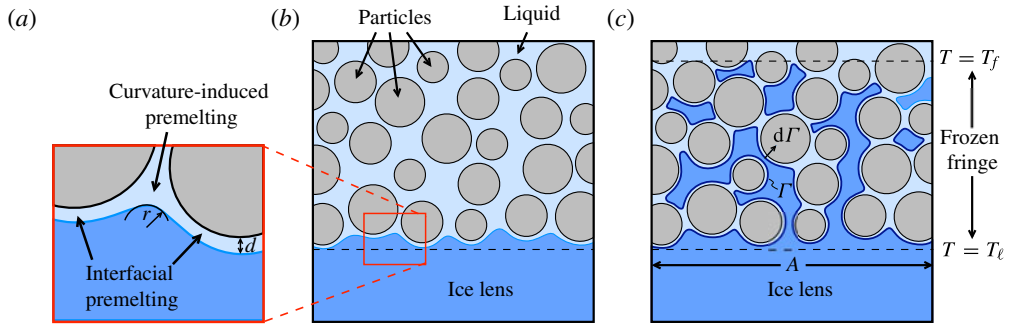


FIGURE 4. (Colour online) (*a*) Freezing point depression in a porous medium arises from curvature near pore throats and interfacial premelting. (*b*,*c*) In order for ice to infiltrate the pore space, the liquid adjacent to the ice lens must be cooled to the ice-entry temperature T_f, which allows a finger of ice extending from the ice lens to pass through a pore throat: (*b*) no pore ice ($T_l > T_f$); (*c*) frozen fringe ($T_l < T_f$).

Aggregation pressures have been measured experimentally for ESCs, giving typical values of $\Pi_c \lesssim 10$ kPa (Meijer, Van Megen & Lyklema 1978; Bensley & Hunter 1983; Goehring *et al.* 2010). The cryostatic suction accompanying ice segregation can easily produce compressive stresses that are several orders of magnitude larger than Π_c, suggesting that aggregation is ubiquitous in freezing colloidal suspensions. Aggregation appears in our mathematical model in two ways. First, at the compaction front, Π_c enters as a dynamic boundary condition that sets the pressure at the top of the compacted layer. In this way, Π_c is analogous to the 'reservoir' pressure adopted in previous frost-heave models; however, whereas previous models arbitrarily fix the position of the reservoir at some distance removed from the freezing zone, in the present case, the location of the compaction front is determined dynamically.

The second way that aggregation enters our model is during ice-lens nucleation. A new ice lens forms by cleaving the particle matrix, a process that must overcome the cohesive strength of the matrix. In principle, the cohesive strength of the particle matrix can be estimated from the interparticle forces (figure 3) and the number of broken particle 'bonds' per unit area along the surface of an incipient ice lens.

2.3. *The frozen fringe*

Water confined within a porous medium remains only partially frozen below the bulk melting temperature T_m. As illustrated in figure 4, the shift in the freezing point of pure water is the result of curved phase boundaries near the throats of pores and interfacial premelting along particle surfaces caused by intermolecular forces between the constituent phases (Cahn, Dash & Fu 1992; Dash, Rempel & Wettlaufer 2006). The relative importance of these two effects is given by a generalized Clapeyron equation (Wettlaufer & Worster 2006)

$$\mathscr{L}\Delta T = \gamma\kappa + p_T(d), \tag{2.1}$$

where $\Delta T = T_m - T$ is the freezing-point shift, κ is the curvature of the phase boundary with radius of curvature centred in the ice phase and $p_T > 0$ is the disjoining pressure arising from intermolecular forces (e.g. repulsive van der Waals forces) in a premelted liquid film of thickness d. The surface energy of the phase boundary is

https://doi.org/10.1017/jfm.2014.500 Published online by Cambridge University Press

denoted by γ and $\mathscr{L} = \rho L/T_m$, where L is the latent heat per unit mass of ice and ρ is the density of ice.

Equation (2.1) predicts the degree of undercooling required for a finger of ice protruding from the ice lens to pass through a pore throat and infiltrate the adjacent pore space. Here, curvature plays a dominant role. Letting R_p denote the radius of a pore throat and substituting $\kappa = 2/R_p$ into (2.1) gives an estimate for the ice-entry temperature

$$T_f = T_m - \frac{2\gamma}{\mathscr{L} R_p}. \tag{2.2}$$

This result neglects interfacial premelting by assuming that $R_p \gg d$, which is a reasonable assumption when the particle size is greater than 100 nm, as in most frost-susceptible soils and in the experiments reported by AW. A pore-ice-bearing fringe forms when the temperature at the leading edge of the warmest ice lens T_ℓ falls below the ice-entry temperature, as illustrated in figure 4(*c*).

An interconnected liquid network is maintained in the frozen fringe due to the persistence of unfrozen water near particle surfaces and in the pendular regions near pore throats, even at large undercoolings. Temperature variations along this premelted network give rise to variations in the disjoining pressure between ice and particles in accordance with (2.1). At a macroscopic level, this thermomolecular pressure gradient pushes the particles towards warmer temperatures and drives the migration of liquid towards colder temperatures to sustain ice-lens growth. This slow exchange of material along the temperature gradient, referred to as thermal regelation, is phenomenologically captured in early 'rigid-ice' models of frost heave (O'Neill & Miller 1985; Fowler 1989). More recently, Rempel *et al.* (2004) reformulated the rigid-ice model from first principles, with direct appeal to premelting dynamics and (2.1). In the next section, we summarize the force equilibrium constraints developed by Rempel *et al.* (2004), which yield the ice-lens growth rate and give the conditions under which new lenses are initiated.

The direct observation of a pore-ice-bearing fringe in experiments on ice-lens formation has proven elusive (Watanabe & Mizoguchi 2000; Peppin & Style 2013) and recent theoretical work by Style *et al.* (2011) has proposed fringe-free mechanisms for ice-lens formation. Though AW do not directly probe for pore ice, the presence of a frozen fringe is consistent with other experimental observations. Specifically, in addition to providing a mechanism for ice-lens initiation and an explanation for the distinct appearance of the undercooled region ahead of the warmest ice lens (light-coloured layer, figure 1), a frozen fringe is consistent with other observations: estimates for the ice-entry temperature (2.2) fell within the range of undercoolings occupied by the light-coloured layer; for a given freezing rate and compacted layer thickness, a frozen fringe, by reducing the permeability of the porous matrix, provides the additional resistance to flow necessary to dissipate all of the cryostatic suction generated at the warmest ice lens. By assuming a frozen fringe, the theory that follows provides a consistent framework for interpreting the experimental observations.

3. Governing equations

3.1. *Rigid-ice model with dynamic reservoir*

Working in the laboratory frame, let z measure the height above the bulk freezing isotherm $T = T_m$ (figure 2). We adopt a frozen-temperature approximation (Davis 2001)

https://doi.org/10.1017/jfm.2014.500 Published online by Cambridge University Press

with fixed temperature gradient G, such that position and temperature in the lab frame are related by

$$T = T_m + Gz. \tag{3.1}$$

The frozen-temperature approximation neglects the effect of latent heat and assumes uniform thermal properties between all of the phases. These assumptions allow us to focus on the dynamics of the compaction front without needing to solve an additional heat equation, and their validity is discussed further in § 5.

Taking $z_c(t)$ and $z_\ell(t)$ to denote the instantaneous positions of the compaction front and the leading edge of the warmest (active) ice lens, respectively, the evolution of these quantities is given by the following kinematic relations:

$$\frac{\mathrm{d}z_\ell}{\mathrm{d}t} = V_\ell(z_\ell, z_c), \quad \frac{\mathrm{d}z_c}{\mathrm{d}t} = V_c(z_\ell, z_c), \tag{3.2a,b}$$

where it remains to determine the growth rates V_ℓ and V_c relative to the laboratory frame of reference.

The compacted layer grows as a result of particle accumulation at z_c, where there is a jump in particle concentration from the bulk value ϕ_0 to the close-packed value ϕ_p. The particle volume balance at z_c gives

$$(\phi_p - \phi_0)V_c = (\phi v_p)|_{z_c{}^-} - (\phi v_p)|_{z_c{}^+}, \tag{3.3}$$

where the volume-averaged particle velocity, v_p, is evaluated on each side of the compaction front to give the required jump in the volume flux of particles. In the bulk suspension, particles translate at the pulling speed: $v_p(z_c{}^+) = -V$. In the compacted layer, the particle velocity matches the growth rate of the ice lens: $v_p(z_c{}^-) = V_\ell$. This latter result follows from the assumptions that the compacted layer is rigid, with a constant particle fraction, and that the ice lens is completely devoid of particles. Substituting these values for v_p into (3.3) yields the growth rate of the compaction front

$$V_c(z_\ell, z_c) = \frac{\phi_p V_\ell(z_\ell, z_c) + \phi_0 V}{\phi_p - \phi_0}. \tag{3.4}$$

Note that when the ice lens is stationary in the laboratory frame ($V_\ell = 0$), the compacted layer continues to grow owing to the supply of particles from the bulk suspension.

The fluid flow induced by ice-lens growth is sufficiently slow that inertia can be ignored. Ice-lens growth is therefore governed by a force-equilibrium constraint. Rigid-ice models derive their name from the assumption that, when a frozen fringe is present, the pore ice and ice lens form a rigid interconnected body of ice – forces that are generated on the surfaces of the pore ice are transmitted directly to the ice lens without deforming the pore-ice network (O'Neill & Miller 1985). The net force on the ice lens is the contribution of stresses over the entire premelted surface of the ice in contact with the particle matrix. There are two primary stresses involved: those arising from viscous flow through the porous matrix and those with a thermomolecular origin, derived from disjoining forces between the ice and particles. In the context of frost heave in soils, overburden stresses produced from the weight of the overlying soil or from an applied load at the surface of the soil are also relevant. With appeal to the experiments in AW, we neglect gravity and any associated overburden, since they are small compared to the thermomolecular stresses.

https://doi.org/10.1017/jfm.2014.500 Published online by Cambridge University Press

First, consider the total thermomolecular force $\boldsymbol{F}_T^{ice}$ acting on a portion of the warmest ice lens with cross-sectional area A. This force is given by an integral over the surface of the ice Γ (see figure 4*c*) directly connected to this portion of the ice lens

$$\boldsymbol{F}_T^{ice} = -\int_\Gamma p_T \mathrm{d}\Gamma = \int_\Gamma (\gamma\kappa - \mathscr{L}\Delta T)\,\mathrm{d}\Gamma, \tag{3.5}$$

where p_T is the disjoining pressure and $\mathrm{d}\Gamma$ is the surface area element with normal directed exterior to the ice. The integral on the right-hand side of this expression was obtained by substituting (2.1). Rempel *et al.* (2004) analysed this latter form directly using the principle of 'thermodynamic buoyancy' (Rempel, Wettlaufer & Worster 2001), which states that the net thermomolecular force is proportional to the volume of ice displaced by the particle matrix. This dramatically simplifies the expression for the thermomolecular stress to

$$P_T^{ice} = \frac{\boldsymbol{F}_T^{ice}\cdot\hat{\boldsymbol{z}}}{A} = -\mathscr{L}G\int_{z_\ell}^{0}(1-\Phi)\,\mathrm{d}z, \tag{3.6}$$

where $\hat{\boldsymbol{z}}$ is the unit coordinate vector directed along the temperature gradient and Φ is the (temperature dependent) volume fraction of ice, discussed in greater detail below. Note that $P_T^{ice} \leqslant 0$, indicating that disjoining forces push the ice lens towards colder temperatures. In the absence of a frozen fringe, where $z_\ell > z_f$ and $\Phi = 0$, the thermomolecular stress is given by $P_T^{ice} = \mathscr{L}Gz_\ell = -\mathscr{L}(T_m - T_\ell)$.

Similarly, the total hydrodynamic force $\boldsymbol{F}_\mu^{ice}$ acting on the same portion A of the ice lens arises from variations of the fluid pressure p over the surface Γ. Rempel *et al.* (2004) used the divergence theorem to simplify the surface integral for $\boldsymbol{F}_\mu^{ice}$ by assuming that the macroscopic pressure gradient is one-dimensional, i.e. $\boldsymbol{\nabla}p = (\mathrm{d}p/\mathrm{d}z)\hat{\boldsymbol{z}}$. Furthermore, since we are only concerned with gradients of the fluid pressure, it is convenient to define p relative to the external pressure, so that $p = -\Pi$, where Π is the compressive stress on the particle matrix (Peppin, Elliott & Worster 2005) (see figure 3). Accounting for the force required to aggregate a portion A of the suspension at the compaction front, it follows that the total hydrodynamic stress on the ice lens is given by

$$P_\mu^{ice} = \frac{\boldsymbol{F}_\mu^{ice}\cdot\hat{\boldsymbol{z}}}{A} = \Pi_c + \int_{z_\ell}^{z_c}\frac{\mathrm{d}p}{\mathrm{d}z}(1-\Phi)\,\mathrm{d}z. \tag{3.7}$$

Fluid flow is assumed to obey Darcy's law $\mu\boldsymbol{u}\cdot\hat{\boldsymbol{z}} = -k(\mathrm{d}p/\mathrm{d}z)$, where $\boldsymbol{u}$ is the Darcy flux, μ is the fluid viscosity and $k = k(\Phi)$ is the pore-ice-dependent permeability, which is discussed in greater detail below. Continuity at $z = z_\ell$ requires $\boldsymbol{u}\cdot\hat{\boldsymbol{z}} = -(1-\Phi)(V + V_\ell)$, so that

$$P_\mu^{ice} = \Pi_c + \mu(V+V_\ell)\int_{z_\ell}^{z_c}\frac{(1-\Phi)^2}{k(\Phi)}\mathrm{d}z. \tag{3.8}$$

Requiring that $z_c > z_\ell$ we have $P_\mu^{ice} \geqslant 0$, indicating that hydrodynamic stresses cause the ice lens to advance towards warmer temperatures.

With the absence of external forces, the opposing hydrodynamic and thermomolecular forces must balance, providing the equilibrium constraint

$$P_T^{ice} + P_\mu^{ice} = 0 \tag{3.9}$$

https://doi.org/10.1017/jfm.2014.500 Published online by Cambridge University Press

on the ice-lens growth rate. Substituting (3.6) and (3.8) into the constraint above gives

$$V_\ell(z_\ell, z_c) = \frac{\mathscr{L}G\int_{z_\ell}^{0}(1-\Phi)\mathrm{d}z - \Pi_c}{\mu\int_{z_\ell}^{z_c} k^{-1}(1-\Phi)^2\mathrm{d}z} - V. \tag{3.10}$$

In order to specify the dynamical system completely, constitutive relations are needed to prescribe the temperature dependence of Φ and k within the frozen fringe. These relations are discussed below.

3.2. *Ice-lens nucleation*

For given ice-lens and compaction front positions, the total stress on the particle matrix $\Pi(z)$ at a position $z > z_\ell$ comes from a combination of thermomolecular and viscous stresses, denoted by Π_T and Π_μ, respectively. We define Π such that $\Pi > 0$ corresponds to a particle matrix in compression and $\Pi < 0$ to tension. Newton's third law ensures that the forces on the particle matrix are equal and opposite to the forces on the ice, so that the same integrals used to derive P_T^{ice} and P_μ^{ice} apply, but for the portion of ice surface above the isotherm at z. Following Rempel *et al.* (2004), the stresses on a horizontal cross-section A are

$$\Pi_T(z) = -\mathscr{L}G\left[(1-\Phi)z + \int_z^0 (1-\Phi)\mathrm{d}z\right] \quad (z_\ell < z < 0), \tag{3.11}$$

which push the particles towards warmer temperatures, and

$$\Pi_\mu(z) = \Pi_c + \mu\,[V + V_\ell(z_\ell, z_c)]\int_z^{z_c}\frac{(1-\Phi)^2}{k(\Phi)}\mathrm{d}z \quad (z_\ell < z < z_c), \tag{3.12}$$

which push the particles towards colder temperatures, in the direction of the flow. Here again, the principle of thermodynamic buoyancy applies to Π_T, with the quantity in square brackets giving the volume of ice displaced by the particle matrix between the isotherm at z and the isotherm for the bulk freezing point. Note that, with z_ℓ and z_c appearing as parameters in the expression for Π_μ, the resulting stress distribution is intrinsically time dependent.

Ice-lens nucleation occurs at a point z_n in the interior of the frozen fringe at the first moment t_n that the thermomolecular stress balances the combination of the hydrodynamic stress and the cohesive strength Σ of the particle matrix. This is determined by

$$\Pi(z_n; z_\ell^\star, z_c^\star) + \Sigma = 0 \quad (z_\ell^\star < z_n < z_f) \tag{3.13}$$

such that

$$\frac{\partial\Pi}{\partial z_n} = 0, \tag{3.14}$$

where $z_{\ell,c}^\star = z_{\ell,c}(t_n)$. When the nucleation conditions above are satisfied, a new ice lens is assumed to form instantaneously and the previous ice lens becomes inactive. Integration of the evolution equations (3.2) is therefore stopped and restarted with new initial conditions $(z_\ell(t_n), z_c(t_n)) = (z_n, z_c^\star)$ until a limit cycle is obtained.

https://doi.org/10.1017/jfm.2014.500 Published online by Cambridge University Press

3.3. *Frozen fringe constitutive relations*

Models (O'Neill & Miller 1985; Cahn *et al.* 1992; Rempel *et al.* 2004) for the ice fraction Φ and permeability k in the frozen fringe are given by relations of the form

$$\Phi = (1-\phi_p)(1-f_L) \quad \text{and} \quad k = k_0 f_L^{\beta/\alpha}, \tag{3.15a,b}$$

where k_0 is the permeability of the ice-free compacted layer, α and β are positive exponents and

$$f_L(T) = \begin{cases} 1 & (T > T_f) \\ \left(\dfrac{T_m - T_f}{T_m - T}\right)^{\alpha} & (T \leqslant T_f) \end{cases} \tag{3.16}$$

is the temperature-dependent liquid fraction occupying the pore space, reflecting the continuous nature of the phase transition in a porous medium.

For simplicity, the exponents α and β are taken as constants. There is some justification for this in the literature. A theoretical examination of f_L by Cahn *et al.* (1992) showed that $\alpha \approx 2$ for moderate undercoolings in the case of ordered packings of monodisperse particles, and they found good agreement with experiments. The physical basis for $\alpha = 2$ is that the vast majority of the liquid resides in the pendular regions near particle contacts, where curvature is the dominant factor in (2.1); only at large undercoolings does the contribution to the liquid fraction from premelted films become important. In more recent theoretical work, which examines random packings and incorporates effects from dissolved impurities (Hansen-Goos & Wettlaufer 2010) and polydispersed particles (Rempel 2012), constant α remains a good approximation for moderate undercoolings, though the predictions give $1 < \alpha < 2$. In the case of the exponent β controlling the permeability, Rempel *et al.* (2004) suggest that $\beta = 4$ based on geometric arguments for the fluid pathways when the majority of the water is located in the pendular regions. In all likelihood, the value of β is system-dependent. For instance, values of β inferred from experimental data compiled for naturally occurring clays and silts are highly variable (Andersland & Ladanyi 2004). O'Neill & Miller (1985) use values $7 \leqslant \beta \leqslant 9$. Based on our own experiments with aggregated alumina, the value was estimated to be $\beta \approx 6$ (see AW). Below, we assess the sensitivity of the model to α and β, along with other parameters that are not well constrained.

3.4. *Non-dimensional system*

The system of equations above is made non-dimensional with the following scales: length $\delta_f = (T_m - T_f)/G$; pressure $\mathscr{L}(T_m - T_f)$; velocity $k_0 \mathscr{L} G/\mu$. Indicating rescaled quantities with hats, we define non-dimensional variables

$$\hat{z} = \frac{z}{\delta_f}, \quad \hat{\Pi} = \frac{\Pi}{\mathscr{L} G \delta_f}, \quad \hat{V}_{\ell,c} = \frac{\mu V_{\ell,c}}{k_0 \mathscr{L} G}, \tag{3.17a–c}$$

such that the ice-entry isotherm is located at $\hat{z} = -1$. Applying this rescaling to (3.4) and (3.10), gives non-dimensional growth rates

$$\hat{V}_\ell(\hat{z}_\ell, \hat{z}_c) = \frac{I_1(\hat{z}_\ell) - \hat{\Pi}_c}{I_2(\hat{z}_\ell, \hat{z}_c)} - \hat{V}, \quad \hat{V}_c(\hat{z}_\ell, \hat{z}_c) = \frac{\phi_p \hat{V}_\ell(\hat{z}_\ell, \hat{z}_c) + \phi_0 \hat{V}}{\phi_p - \phi_0}, \tag{3.18a,b}$$

https://doi.org/10.1017/jfm.2014.500 Published online by Cambridge University Press

where I_1 and I_2 are integrals defined by

$$I_1(x) = \int_x^0 [\phi_p + (1-\phi_p) f_L(\hat{z})] \mathrm{d}\hat{z}, \tag{3.19}$$

$$I_2(x, y) = \int_x^y f_L^{-\beta/\alpha} [\phi_p + (1-\phi_p) f_L(\hat{z})]^2 \mathrm{d}\hat{z} \tag{3.20}$$

and

$$f_L(\hat{z}) = \begin{cases} 1, & (\hat{z} > -1) \\ |\hat{z}|^{-\alpha}, & (\hat{z} \leqslant -1) \end{cases} \tag{3.21}$$

is the liquid fraction, rewritten in terms of $\hat{z}$. Rescaling the nucleation conditions (3.13) and (3.14) gives

$$\hat{z}_n \frac{\partial}{\partial \hat{z}_n} I_1(\hat{z}_n) - I_1(\hat{z}_n) + [\hat{V} + \hat{V}_\ell(\hat{z}_\ell, \hat{z}_c)] I_2(\hat{z}_n, \hat{z}_c) + \hat{\Pi}_c + \hat{\Sigma} = 0 \tag{3.22}$$

and

$$\hat{z}_n \frac{\partial^2}{\partial \hat{z}_n^2} I_1(\hat{z}_n) + [\hat{V} + \hat{V}_\ell(\hat{z}_\ell, \hat{z}_c)] \frac{\partial}{\partial \hat{z}_n} I_2(\hat{z}_n, \hat{z}_c) = 0 \tag{3.23}$$

respectively. In addition to the parameters α and β, the non-dimensional parameters appearing above are

$$\hat{V} = \frac{\mu V}{k_0 \mathscr{L} G}, \quad \hat{\Pi}_c = \frac{\Pi_c}{\mathscr{L} G \delta_f}, \quad \hat{\Sigma} = \frac{\Sigma}{\mathscr{L} G \delta_f}, \tag{3.24a–c}$$

which define a non-dimensional pulling speed, aggregation pressure, and cohesive strength, respectively.

4. Results

4.1. *Fixed versus dynamic reservoir*

First, consider a scenario where the position of the compaction front is fixed in the laboratory frame, i.e. where $\hat{V}_c = 0$, which is equivalent to the case of a fixed reservoir considered in previous frost-heave models (O'Neill & Miller 1985; Fowler 1989; Rempel *et al.* 2004; Rempel 2007). Although this scenario is artificial, it allows us to summarize the main features of the model before moving on to the more general case to assess the dynamical significance of an evolving compaction front. In the present notation, the reservoir is located at $\hat{z}_c$ and has pressure $\hat{\Pi}_c$. By considering here the case of a reservoir in hydrostatic equilibrium, such that $\hat{\Pi}_c = 0$, and where the particle matrix is cohesionless, such that $\hat{\Sigma} = 0$, we recover the solutions obtained by Rempel *et al.* (2004).

The ice-lens growth rate is plotted as a function of ice-lens position for three different values of $\hat{z}_c$ in figure 5(*a*). Recall that as $\hat{z}_\ell$ decreases, the leading edge of the ice lens becomes colder. When $\hat{z}_\ell$ falls below the ice-entry isotherm, located at $\hat{z} = -1$, the ice lens grows with a frozen fringe precursor. According to (2.1), the cryostatic suction generated by the ice lens is proportional to the undercooling, that is $\Delta p \sim \mathscr{L} \Delta T$. Consequently, the driving force for growth increases as the ice lens cools below the bulk freezing point. This produces an initial increase in $\hat{V}_\ell$ with

https://doi.org/10.1017/jfm.2014.500 Published online by Cambridge University Press

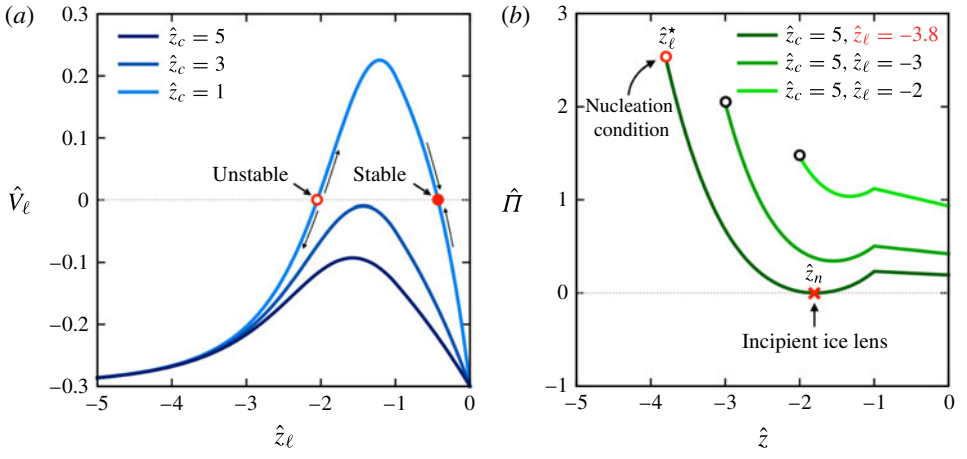


FIGURE 5. (Colour online) Fixed reservoir solutions (Rempel *et al.* 2004). (*a*) The ice-lens growth rate is shown for three values of $\hat{z}_c$. Larger values of $\hat{z}_c$ reduce the maximum achievable growth rate $\hat{V}_{\ell,max}$ due to the enhanced resistance to flow in the compacted layer. When $\hat{V}_{\ell,max} > 0$ (e.g. $\hat{z}_c = 1$), the (stable) steady state, where $\hat{V}_\ell = 0$, results in the sustained growth of a single ice lens. When $\hat{V}_{\ell,max} < 0$ (e.g. $\hat{z}_c = 5$), the ice lens retreats to colder temperatures, developing a frozen fringe precursor, until a new ice lens is nucleated and the process repeats, leading to periodic ice lenses. (*b*) Instantaneous distributions of the matrix stress for three ice-lens positions, where $\hat{z}_c = 5$. The stress distribution is non-monotonic in the frozen fringe $\hat{z} < -1$ due to thermomolecular forces. When the fringe becomes sufficiently thick ($\hat{z}_\ell = 3.8$), a new ice lens is nucleated. For a cohesionless matrix, the new ice lens emerges where $\hat{\Pi} = 0$. (Parameter values: $\hat{V} = 0.3$, $\hat{\Pi}_c = 0$, $\hat{\Sigma} = 0$, $\alpha = 2$, $\beta = 4$.)

decreasing $\hat{z}_\ell$; however, when a frozen fringe develops at yet colder temperatures, the driving force for flow is counteracted by a significant reduction in the permeability through the ice-filled pore space, such that $\hat{V}_\ell \to -\hat{V}$ as $\hat{z}_\ell \to -\infty$. These competing factors lead to a maximum growth rate $\hat{V}_{\ell,max}$ near $\hat{z}_\ell = -1$.

Although a significant portion of the cryostatic suction is dissipated by flow in the frozen fringe, the resistance to flow in the unfrozen portion of the compacted layer has a non-negligible effect on the ice-lens growth. Larger values of $\hat{z}_c$ result in smaller values of $\hat{V}_{\ell,max}$ and, depending on the thickness of the compacted layer, it is possible to have $\hat{V}_{\ell,max} > 0$ or $\hat{V}_{\ell,max} < 0$, each of which lead to different long-time behaviours. When $\hat{V}_{\ell,max} > 0$ ($\hat{z}_c = 1$, figure 5*a*), two steady states are possible, where $\hat{V}_\ell = 0$. The state with the warmer ice lens is stable, which corresponds to the sustained growth of a single ice lens. When $\hat{V}_{\ell,max} < 0$ ($\hat{z}_c = 5$, figure 5*a*), there are no longer any stationary solutions, since the rate that liquid is supplied to the ice lens is insufficient to keep pace with the advancing isotherms. The ice lens continuously retreats towards colder temperatures and forms a frozen fringe precursor which gradually thickens and eventually spawns a new ice lens. The ice-lens nucleation process is illustrated in figure 5(*b*) for the case $\hat{z}_c = 5$, where instantaneous stress distributions in the particle matrix are shown for three successive values of $\hat{z}_\ell$. These non-monotonic stress distributions have a local minimum $\hat{\Pi}_{min}$ in the interior of the frozen fringe, owing to thermomolecular forces between the ice and particles. According to (3.13) and (3.14),

https://doi.org/10.1017/jfm.2014.500 Published online by Cambridge University Press

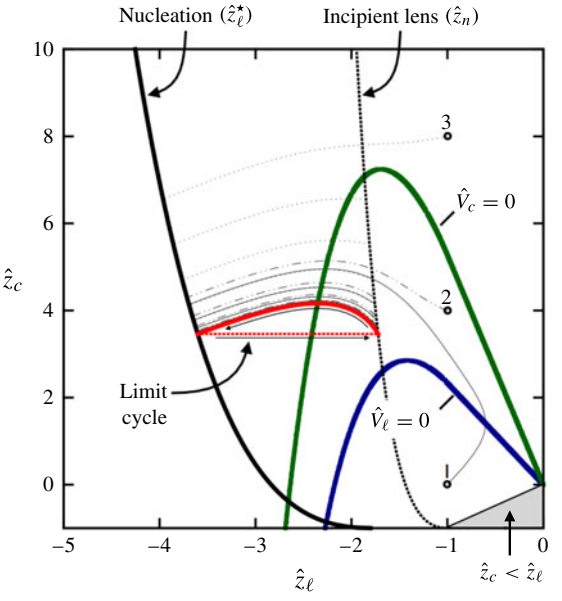


FIGURE 6. (Colour online) Ice-lens growth with an evolving compaction front (dynamic reservoir). Trajectories are plotted in the $(\hat{z}_\ell, \hat{z}_c)$ phase plane for three initial conditions (thin light grey curves), labelled 1, 2 and 3. Important regions of the phase plane are demarcated by heavy solid lines: $\hat{V}_\ell = 0$, $\hat{V}_c = 0$, and ice-lens nucleation conditions ((3.13) and (3.14)), labelled accordingly. The loci of incipient ice-lens positions are also shown (black dashed). A trajectory which intercepts $\hat{z}_\ell^\star$ re-emerges at $\hat{z}_n$, producing oscillations between ice-lens nucleation events that converge to a unique limit cycle. Single-ice-lens solutions found for the fixed reservoir case only exist as a transient state (e.g. trajectory 1). Parameter values are $\hat{V} = 0.3$, $\hat{\Pi}_c = 0$, $\hat{\Sigma} = 0$, $\alpha = 2$, $\beta = 4$, $\phi_0 = 0.3$.

once the ice lens has retreated to a sufficient depth $\hat{z}_\ell^\star$, a new ice lens is initiated at the position $\hat{z}_n$, coinciding with $\hat{\Pi}_{min} = 0$ for a cohesionless particle matrix. When the new lens is initiated, the process repeats, to produce a periodic sequence of ice lenses with inter-lens spacing given by $\hat{z}_n - \hat{z}_\ell^\star$.

The discussion above highlights the importance of the compacted layer in mediating ice-lens growth. Allowing for an evolving compaction front necessarily modifies the long-time freezing behaviour. Recalling figure 2, the growth of a single ice lens is no longer observed as a steady state due to the continuous supply of particles from the bulk suspension. The duration of this transient state is controlled by the growth rate of the compacted layer; $\hat{V}_{\ell,max}$ inevitably becomes negative and periodic ice-lensing ensues. In predicting the resulting limit cycle, the oscillations in the position of the compaction front between successive ice-lens nucleation events become important. Indeed, we discuss later how these oscillations in $\hat{z}_c$ lead to a breakdown of the periodic-ice-lensing state at high pulling speeds.

Phase-plane trajectories $(\hat{z}_\ell, \hat{z}_c)$ are shown in figure 6 for the same parameter values as in the fixed-reservoir case. The curves for $\hat{V}_\ell = 0$ and $\hat{V}_c = 0$ partition the phase plane into three regions from which initial conditions (points 1, 2 and 3) were chosen for the trajectories shown. The loci of points $(\hat{z}_\ell^\star, \hat{z}_c)$ and $(\hat{z}_n, \hat{z}_c)$ obtained from the ice-lens initiation criteria, (3.13) and (3.14), are also included in the phase plane. When a trajectory reaches the point $(\hat{z}_\ell^\star, \hat{z}_c)$, a new ice lens is activated, and the trajectory

https://doi.org/10.1017/jfm.2014.500 Published online by Cambridge University Press

re-emerges at the point $(\hat{z}_n, \hat{z}_c)$. The resulting oscillations ultimately converge to a limit cycle, which is the unique attractor for all trajectories in the phase plane. In the next section, we examine features of the limit cycle as the system parameters are varied.

4.2. *Periodic ice lenses*

In a series of freezing experiments with alumina suspensions, varying only the pulling speed, AW measured the steady-state thickness of the compacted layer and ice-lens characteristics (spacing and thickness). We compare these experimental observations against theoretical predictions, by computing the limit cycle for a range of $\hat{V}$. For the steady-state thickness of the compacted layer $\hat{H}$, we compute the time-averaged value of $\hat{z}_c - \hat{z}_\ell$ over the entire cycle. The ice-lens spacing ($\hat{\lambda}_s$) and thickness ($\hat{\lambda}_t$) are given by

$$\hat{\lambda}_s = \hat{z}_n - \hat{z}_\ell^\star, \quad \hat{\lambda}_t = \int_{\hat{t}_n}^{\hat{t}_\ell^\star} (\hat{V}_\ell + \hat{V}) \mathrm{d}\hat{t} = \hat{V}(\hat{t}_\ell^\star - \hat{t}_n) - \hat{\lambda}_s, \tag{4.1a,b}$$

where $\hat{t}_n$ is the time when the ice lens is initiated at position $\hat{z}_n$ and $\hat{t}_\ell^\star$ is the time when the ice lens reaches depth $\hat{z}_\ell^\star$ and the next ice lens is initiated. These calculations are shown in figure 7. The experimental measurements were made non-dimensional using the following parameter values: $G = 6$ K cm^{-1}, $T_m - T_f = 0.5$ K, $\mathscr{L} = 1.1 \times 10^6$ Pa K^{-1}, $\mu = 1.8 \times 10^{-3}$ Pa s and $k_0 = 2 \times 10^{-13}$ cm^2.

Recalling figure 1, three regimes of ice segregation were observed in the experiments, depending on the value of $\hat{V}$. The intervals of $\hat{V}$ for the three experimental regimes are identified in figure 7(*b*) as I, II and III. At low pulling speeds (I), regular periodic ice lenses were observed, which are accompanied by a compacted layer of appreciable thickness. At moderate pulling speeds (II), over a relatively narrow range of $\hat{V}$, a new regime emerges where the extent of the compacted layer is considerably diminished and the pattern of ice lensing disordered. These two regimes of ice-lens formation are replaced at higher pulling speeds (III) by a new mode of ice segregation, which has a periodic banded structure that is qualitatively different from ice lenses. Furthermore, there is no visible compacted layer in this latter regime.

The theoretically obtained results also exhibit three regimes. For the smallest values of $\hat{V}$, the limit cycle has a single mode of ice-lens formation (figure 7*c*), just as in the experiments. The computed values of $\hat{H}$, $\hat{\lambda}_t$ and $\hat{\lambda}_s$ in this regime (figure 7*a,b*) have a power-law dependence on $\hat{V}$ that is qualitatively similar to the experimental measurements. In the case of $\hat{H}$, there is good quantitative agreement with the experiments for the chosen parameter values. The quantitative discrepancy in the prediction of the ice-lens characteristics may be due to poorly constrained parameters, as discussed further below. Over an intermediate range of $\hat{V}$, the limit cycle has two modes of ice-lens formation (figure 7*d*). The transition to bimodal oscillations is also apparent from the multiple values of $\hat{\lambda}_t$ and $\hat{\lambda}_s$ for a given $\hat{V}$, with an appreciable difference in the thickness of the ice lenses between the two modes of the limit cycle. Finally, above some critical value of $\hat{V}$, marked by the termination of the curves in figure 7, the regime for ice-lens formation breaks down. The cause of the breakdown is that the oscillating compaction front intercepts the leading edge of the frozen fringe (i.e. $\hat{z}_c = -1$) before a limit cycle can be reached (figure 7*e*). When this event occurs, ice nuclei

https://doi.org/10.1017/jfm.2014.500 Published online by Cambridge University Press

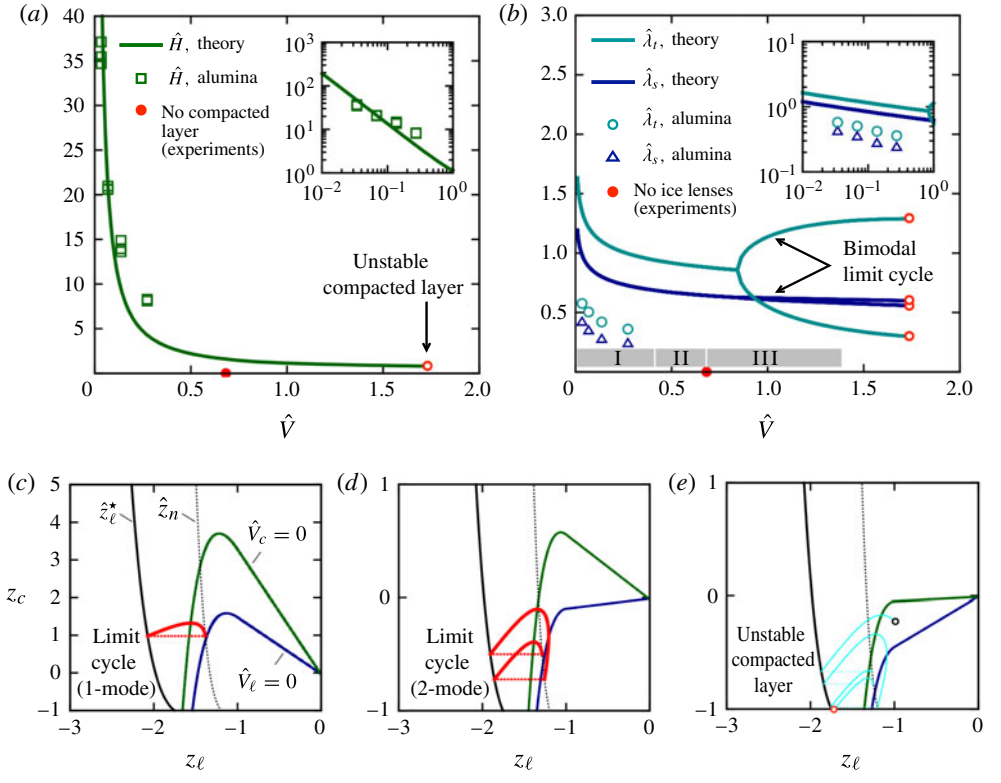


FIGURE 7. (Colour online) Effect of $\hat{V}$ on periodic-state observables: (*a*) $\hat{H}$, thickness of compacted layer ($\hat{z}_c - \hat{z}_\ell$) time-averaged over a limit cycle; (*b*) ice-lens thickness ($\hat{\lambda}_t$) and spacing ($\hat{\lambda}_s$). Log-scale plots are shown in the insets. The open symbols are measurements obtained from alumina experiments (AW). There are three experimental regimes: periodic ice lenses (I), disordered ice lenses (II), and no ice lenses (III). The red point on the $\hat{V}$-axis marks the point in the experiments beyond which there is no visible compacted layer and ice lenses are not observed. There are three theoretical regimes, each exemplified by phase-plane plots: (*c*) 1-mode limit cycle $\hat{V} = 0.4$; (*d*) multi-modal limit cycle $\hat{V} = 1.1$; (*e*) unstable compaction layer $\hat{V} = 1.8$. At high pulling speeds, the oscillating compaction front intercepts the leading edge of the frozen fringe (open red circle), with bimodal oscillations occurring before the compacted layer becomes unstable. Further mode-doubling and chaos can result in this intermediate regime, depending on parameter values (see figure 9). Here, the results are based on the following parameters: $\hat{\Pi}_c = 0.01$, $\hat{\Sigma} = 0.05$ $\phi_0 = 0.27$, $\alpha = 2$, $\beta = 8$.

in the frozen fringe come into contact with an undercooled bulk suspension, which would cause it to freeze, consequently producing a new form of ice segregation.

The regime for multi-modal ice lenses and the eventual breakdown of the compacted layer are discussed further in the next section, where we show that several mode-doubling bifurcations and even chaos can occur at intermediate freezing rates, before the breakdown of the ice-lens regime. For now, we focus on the first ice-lensing regime. Although the trends in $\hat{\lambda}_t$ and $\hat{\lambda}_s$ with $\hat{V}$ are consistent with the experimental observations, the theoretical predictions for the ice-lens thickness and

https://doi.org/10.1017/jfm.2014.500 Published online by Cambridge University Press

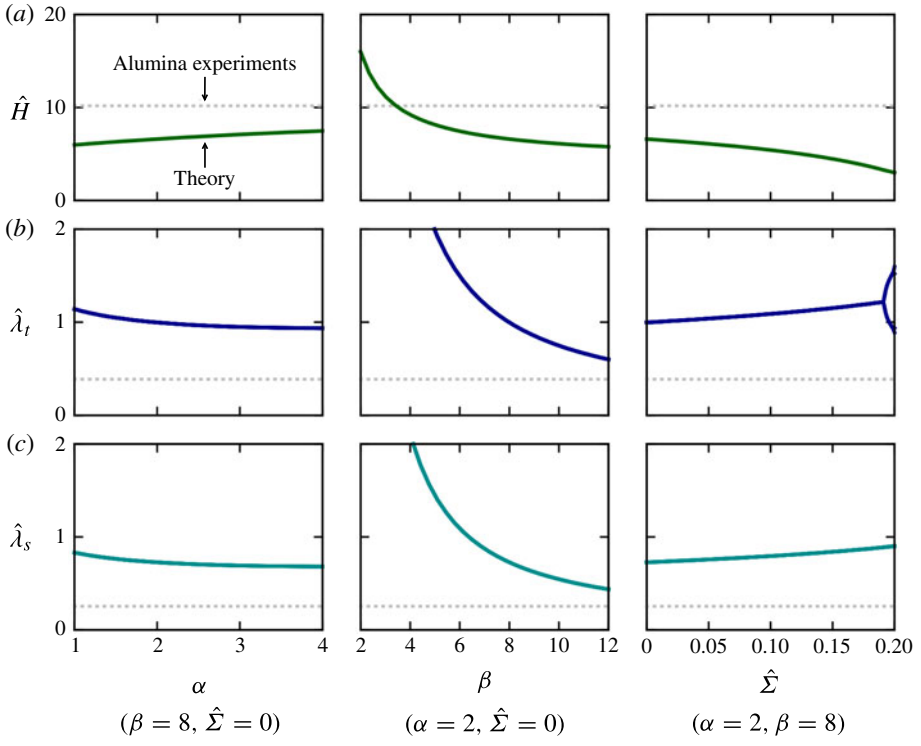


FIGURE 8. (Colour online) Parametric sensitivity of periodic-state observables: $\hat{H}$ (*a*), $\hat{\lambda}_t$ (*b*), $\hat{\lambda}_s$ (*c*). The response of these observables to α, β and $\hat{\Sigma}$ is given in each column; all other parameters are fixed ($\hat{V} = 0.2$, $\hat{\Pi}_c = 0.01$, $\phi_0 = 0.27$). Experimental measurements for alumina (AW) are indicated with a broken grey line.

spacing in figure 7 are greater than the experimental measurements by approximately a factor of 3. This quantitative discrepancy could in part stem from uncertainty in the values of some of the parameters, in particular, α, β and $\hat{\Sigma}$. To examine this possibility, the results of a sensitivity analysis for these parameters are summarized in figure 8, where the value $\hat{V} = 0.2$ was chosen, with all other parameters taking the same values as in figure 7.

The exponent α controlling the liquid fraction f_L in the frozen fringe is fairly well constrained by $1 \leqslant \alpha \leqslant 2$ for moderate undercoolings (see the discussion following (3.16)). Even outside this range, α has only a modest effect on the predictions. Values for the exponent β controlling the permeability in the frozen fringe are not well constrained and yet the predictions are sensitive to this parameter, with $\hat{H}$, $\hat{\lambda}_t$ and $\hat{\lambda}_s$ each decreasing monotonically for $2 \leqslant \beta \leqslant 12$; the ice-lens characteristics decrease by an order of magnitude over this range. Physically speaking, as the frozen fringe becomes more impermeable to flow for larger values of β, it becomes thinner (on average) and dissipates a greater portion of the cryostatic suction, such that a smaller pressure drop occurs over the unfrozen portion of the compacted layer. A thinner frozen fringe results in smaller ice-lens dimensions and partially contributes to smaller $\hat{H}$, although this latter response to β is largely the result of a thinner unfrozen compacted layer and the reduced resistance to flow therein. Finally, for increasing

https://doi.org/10.1017/jfm.2014.500 Published online by Cambridge University Press

values of the parameter $\hat{\Sigma}$ controlling the cohesive strength of the particle matrix, $\hat{\lambda}_t$ and $\hat{\lambda}_s$ increase slightly, while the thickness of the compacted layer decreases. Ice-lens initiation in a more cohesive particle matrix requires a thicker frozen fringe, leading to larger ice-lens dimensions. Moreover, with a thicker fringe, a greater portion of the cryostatic suction is dissipated in the pore-ice-filled matrix, leading on average to smaller $\hat{z}_c$. It is difficult to constrain $\hat{\Sigma}$; however, we see that for values approaching $\hat{\Sigma} = 0.2$, there is a transition to bimodal ice lenses and a large deviation in the prediction of $\hat{H}$ from the experimental observations.

The experimental measurements included in figures 7 and 8 illustrate that, while it is possible to obtain good agreement in the prediction of the compacted layer thickness, there is persistent quantitative disagreement in the prediction of the ice-lens characteristics over a wide range of parameter values. We return to this point later in the Discussion section, where we identify possible sources for this discrepancy between theory and experiment. Nevertheless, the predictions demonstrate the importance of the compacted layer in the experimental observations. In the next section, we focus on the role that the compacted layer plays in controlling the breakdown of periodic ice lenses at high pulling speeds.

4.3. *Breakdown of periodic ice lenses*

The eventual breakdown of the regime for periodic ice lenses is a consequence of the diminishing thickness of the compacted layer at increased freezing rates. Formally, we identify a critical value of $\hat{V}$ where breakdown occurs, as the value where the compaction front intercepts the leading edge of the frozen fringe before the solution trajectory reaches a limit cycle, since the event would nucleate ice growth in the supercooled bulk suspension, which cannot be described with the present model. Moreover, as a result of the oscillations of the compaction front, which are coupled to the repeated generation of new ice lenses, there are interesting transitions in the periodicity leading up to the breakdown. The richness of the behaviour is illustrated in figure 9, which displays plots of the ice-lens thickness and the minimum and maximum values of $\hat{z}_c$ between successive ice-lens nucleation events as $\hat{V}$ is varied. Results are produced for three different values of the cohesive strength $\hat{\Sigma}$.

Multiple modes of periodic ice lenses, where the thickness of the ice lenses alternates between large and small values, are a common feature for each of the cases in figure 9. The source of these multiple modes can be understood by referring to the limit cycles in figure 7(*c*,*d*). For a limit cycle with a single mode, the point $(\hat{z}_n, \hat{z}_c)$ in the phase plane that marks the position where new ice lenses are initiated in the cycle, is at a point where $\hat{V}_\ell \leqslant 0$. By increasing the freezing rate, the point $(\hat{z}_n, \hat{z}_c)$ can cross the curve for $\hat{V}_\ell = 0$ under certain conditions, thereby splitting the limit cycle into two modes: the ice lenses nucleated at the point $\hat{V}_\ell > 0$ (to the right of the curve) grow to be thicker than their predecessors. In the fixed-reservoir case analysed by Rempel *et al.* (2004), the point where $\hat{V}_\ell(\hat{z}_n, \hat{z}_c) = 0$ is an unstable fixed point (figure 5*a*) that separates the periodic-ice-lens and single-ice-lens regimes, leading to hysteresis between these two states. When there is an evolving compacted layer, this hysteresis is removed and instead replaced by mode-doubling.

For the cohesionless particle matrix, bimodal ice lenses occur over a small range of $\hat{V}$ in figure 9 ($\hat{\Sigma} = 0$); these two modes coalesce before breakdown occurs. For larger values of $\hat{\Sigma}$, the window for multi-modal ice lenses expands, beginning at smaller values of $\hat{V}$ and extending beyond the point of breakdown, which is also

https://doi.org/10.1017/jfm.2014.500 Published online by Cambridge University Press

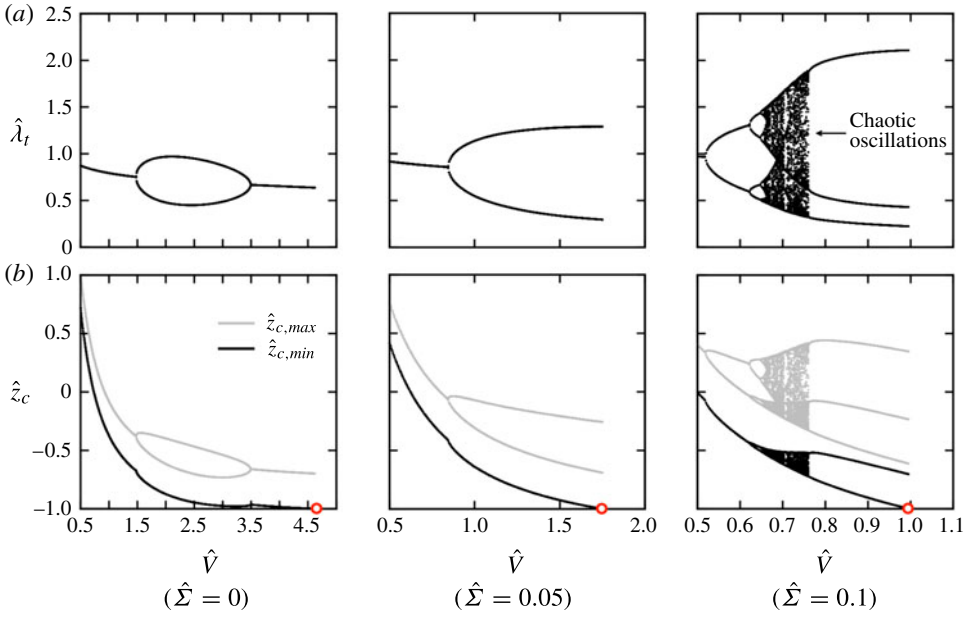


FIGURE 9. (Colour online) Multi-modal limit cycles and the breakdown of sustained ice-lens formation. The ice-lens thickness (a) and minimum and maximum values of $\hat{z}_c$ (b) are plotted, with values for the cohesive strength $\hat{\Sigma}$ increasing from left to right. The point of breakdown, indicated by the circle, occurs when the compaction front intercepts the frozen fringe, i.e. $\hat{z}_{c,min} = -1$. A window of chaos is observed for $\hat{\Sigma} = 0.1$, resulting from a cascade of mode-doubling bifurcations. Parameters values: $\alpha = 2$, $\beta = 8$, $\hat{\Pi}_c = 0.01$, $\phi_0 = 0.27$.

shifted to smaller values of $\hat{V}$. Mode-doubling is particularly prevalent for $\hat{\Sigma} = 0.1$. Here, a sequence of mode-doubling bifurcations generates a cascade into chaotic ice-lens generation, which exists over a finite range of $\hat{V}$. When the chaos subsides, a 3-mode limit cycle remains up until the point of breakdown. The disordered nature of the ice lenses observed experimentally at intermediate freezing rates could be a manifestation of multimodal and, in some instances, chaotic oscillations. At larger values of the cohesive strength, where chaotic oscillations are computed, the range of $\hat{V}$ over which multi-modal oscillations are predicted coincides more closely with the experimental range of the disordered ice lenses (Regime II, figure 7*b*). Further discussion of this connection is given in the next section.

5. Discussion

In this article, the one-dimensional frost-heave model developed by Rempel *et al.* (2004) was extended to include an evolving compaction front that separates a homogeneous colloidal suspension in the bulk from the region of ice-lens growth, and which is the site of a stress-induced sol–gel transition. The resulting close-packed layer imparts viscous resistance to the transfer of water from the bulk suspension to the freezing zone and possesses a cohesive strength that curtails the initiation of new ice lenses. The extended model consists of two coupled ODEs for the growth of the compacted layer and the active ice lens along with nucleation conditions

https://doi.org/10.1017/jfm.2014.500 Published online by Cambridge University Press

for ice-lens initiation. By computing the limit cycles of this dynamical system, we obtained solutions corresponding to periodic ice lenses along with an explanation for the breakdown of these solutions, and have compared these predictions against directional solidification experiments performed by Anderson & Worster (2012).

In directional solidification experiments, the compacted layer is developed *in* situ, which provides a convenient means of studying frost heave and ice-lens formation. Since the thickness of the compacted layer is set dynamically, the coupling between the ice-lens growth kinetics and the position of the compaction front must be considered in order to make direct comparisons between theory and experiment. Measurements of ice-lens growth rates in previous directional solidification experiments on silica suspensions have not considered the compacted layer (Watanabe 2002). Moreover, when describing freezing experiments on fully consolidated suspensions (e.g. Taber 1929), frost-heave models require the location of a 'reservoir', which provides the supply of water for ice-lens growth. Frost-heave models typically fix the position of the reservoir (O'Neill & Miller 1985; Fowler 1989; Rempel *et al.* 2004; Rempel 2007), for example, at the leading edge of the frozen fringe (frost line). In § 4.1, we showed that this assumption results in an incorrect accounting of the resistance to flow in the unfrozen suspension and, in some cases, produces incorrect predictions of the long-time frost-heave behaviour.

In § 4.2, we compared the periodic states computed from our model against experimental measurements reported by Anderson & Worster (2012) for ice-lens characteristics and compaction layer thicknesses in alumina suspensions at freezing rates where the compaction front is well separated from the freezing zone and the ice-lens formation is periodic. The trends in these measured observables as the freezing rate is varied are reproduced by our model. The predictions were found to be sensitive to the parameters controlling the permeability in the frozen fringe (β) and the cohesive strength of the particle matrix ($\hat{\Sigma}$), both of which are not yet well constrained. Within sensible ranges for these parameter values, good quantitative agreement was obtained in the prediction of the compacted layer; however, the quantitative agreement in the prediction of the ice-lens thickness and spacing was at best fair, as the model overestimates these latter observables by approximately a factor of 3 over the range of freezing rates considered.

This quantitative discrepancy may arise in part from simplifying assumptions made in the model. Style & Peppin (2012) discuss 'kinetic effects' arising from additional viscous dissipation in the premelted films in contact with the active ice lens. Though these effects are most relevant in fringe-free models, the additional viscous dissipation in premelted films may indeed play a role even when significant drag is provided by a frozen fringe. Another potential source of discrepancy is the assumption of a constant, uniform temperature gradient, which ignores complications from thermal effects, like differences in the thermal properties between the constituent materials and latent heat release. In fact, the alumina system used by Anderson & Worster (2012) has widely disparate thermal properties; for instance, the thermal conductivities of ice and alumina are 2 and 35 W m^{-1} K^{-1}, respectively, leaving the possibility for significant heat transfer heterogeneities precisely where the ice and suspension are segregated. This issue could be addressed in future experiments with a different choice of particle. As for latent heat release, this can be accounted for by adding a heat equation to the model; the necessary details are provided by Rempel (2007). At this point, it is difficult to assess the impact of these effects on ice-lens formation.

Given the assumptions of the model, we obtain a theoretical framework that provides an explanation for the three regimes of ice segregation in the experiments.

https://doi.org/10.1017/jfm.2014.500 Published online by Cambridge University Press

At intermediate freezing rates, where periodic ice lenses transition to disordered ice lenses in the experiments, the model predicts a transition from a single mode to multiple modes of ice-lensing, and, in some cases, even chaotic oscillations. Theoretically, multiple modes arise from a mode-splitting mechanism, which is related to the existence of an unstable fixed point (and hysteresis, Rempel *et al.* 2004) separating the single-ice-lens and periodic-ice-lens states in the case of a fixed compaction front (§ 4.1, figure 5). In the case of a dynamic compaction front, the unstable fixed point is removed and the single-ice-lens state becomes the thicker of the two ice lenses when the limit cycle splits. The freezing rate ($\hat{V}$) where multiple modes are first obtained was shown to be sensitive to the cohesive strength of the compacted layer ($\hat{\Sigma}$). For the value $\hat{\Sigma} = 0.1$, the first mode-doubling bifurcation occurs at $\hat{V} \approx 0.5$, in close agreement with the experimentally observed transition at $\hat{V} \approx 0.4$. Moreover, for this value of $\hat{\Sigma}$, chaotic oscillations are predicted. These features of the model are driven by oscillations of the compaction front coupled to cyclic ice-lens formation, and we propose this to be one of the drivers of the disordered ice segregation in the experimental observations.

Disordered ice lenses eventually give way to a new form of banded ice segregation at high freezing rates. Theoretically, we predict this transition to occur when the compaction front intercepts the leading edge of the frozen fringe at the ice-entry isotherm, at which point ice would invade the bulk suspension. Other factors not considered in our model may cause this transition to occur at lower freezing rates. For instance, the pattern of ice segregation in the regime of disordered ice lenses exhibits horizontal variations that are not included in this model. Another factor may arise from the observation that the position of the compaction front in steady state is predicted to reside below the isotherm for the bulk freezing point over an appreciable range of freezing rates below where breakdown is predicted. The resulting undercooling of the bulk suspension may lead to morphological instabilities like those predicted by Peppin *et al.* (2008*b*). Horizontal modulations of the ice segregation pattern arising from such instabilities could explain what appear to be dendritic ice crystals in the particle rich bands at high freezing rates (Anderson & Worster 2012), while the overall periodicity of the banding in this regime could be inherited from dynamics described herein. Such factors require further study. The one-dimensional model presented in this article would provide a basic state for such a study.

Acknowledgements

A.M.A. acknowledges that this work was supported by funding from the Leverhulme Trust (Early Career Fellowship) and Isaac Newton Trust, University of Cambridge. This work has also benefited from invaluable discussions with S. Peppin, R. Style and S. Deville.

REFERENCES

ANDERSLAND, O. B. & LADANYI, B. 2004 *Frozen Ground Engineering*. John Wiley & Sons.

ANDERSON, A. M. & WORSTER, M. G. 2012 Periodic ice banding in freezing colloidal dispersions. *Langmuir* **28** (48), 16512–16523.

BENSLEY, C. N. & HUNTER, R. J. 1983 The coagulation of concentrated colloidal dispersions at low electrolyte concentrations: II. Experimental coagulation pressures. *J. Colloid Interface Sci.* **92** (2), 448–462.

https://doi.org/10.1017/jfm.2014.500 Published online by Cambridge University Press

CAHN, J. W., DASH, J. G. & FU, H. 1992 Theory of ice premelting in monosized powders. *J. Cryst. Growth* **123** (1), 101–108.

DASH, J. G., REMPEL, A. W. & WETTLAUFER, J. S. 2006 The physics of premelted ice and its geophysical consequences. *Rev. Mod. Phys.* **78** (3), 695–741.

DAVIS, S. H. 2001 *Theory of Solidification*. Cambridge University Press.

DEVILLE, S., MAIRE, E., BERNARD-GRANGER, G., LASALLE, A., BOGNER, A., GAUTHIER, C., LELOUP, J. & GUIZARD, C. 2009 Metastable and unstable cellular solidification of colloidal suspensions. *Nat. Mater.* **8** (12), 966–972.

DEVILLE, S., SAIZ, E., NALLA, R. K. & TOMSIA, A. P. 2006 Freezing as a path to build complex composites. *Science* **311** (5760), 515–518.

FOWLER, A. C. 1989 Secondary frost heave in freezing soils. *SIAM J. Appl. Maths* **49** (4), 991–1008.

FRENCH, H. M. 2007 *The Periglacial Environment*. John Wiley & Sons.

GOEHRING, L., CLEGG, W. J. & ROUTH, A. F. 2010 Solidification and ordering during directional drying of a colloidal dispersion. *Langmuir* **26** (12), 9269–9275.

HANSEN-GOOS, H. & WETTLAUFER, J. S. 2010 Theory of ice premelting in porous media. *Phys. Rev.* E **81** (3), 031604.

ISRAELACHVILI, J. N. 2011 *Intermolecular and Surface Forces*. 3rd edn. Academic Press.

MAZUR, P. 1984 Freezing of living cells: mechanisms and implications. *Am. J. Physiol. Cell Physiol.* **247**, 125–142.

MEIJER, A. E. J., VAN MEGEN, W. J. & LYKLEMA, J. 1978 Pressure-induced coagulation of polystyrene latices. *J. Colloid Interface Sci.* **66** (1), 99–104.

O'NEILL, K. & MILLER, R. D. 1985 Exploration of a rigid ice model of frost heave. *Water Resour. Res.* **21** (3), 281–296.

PEPPIN, S. S. L., ELLIOTT, J. A. W. & WORSTER, M. G. 2005 Pressure and relative motion in colloidal suspensions. *Phys. Fluids* **17** (5), 053301.

PEPPIN, S. S. L., ELLIOTT, J. A. W. & WORSTER, M. G. 2006 Solidification of colloidal suspensions. *J. Fluid Mech.* **554**, 147–166.

PEPPIN, S. S. L., HUPPERT, H. E. & WORSTER, M. 2008*a* Steady-state solidification of aqueous ammonium chloride. *J. Fluid Mech.* **599**, 465–476.

PEPPIN, S., MAJUMDAR, A., STYLE, R. & SANDER, G. 2011 Frost heave in colloidal soils. *SIAM J. Appl. Maths* **71** (5), 1717–1732.

PEPPIN, S. S. L. & STYLE, R. W. 2013 The physics of frost heave and ice-lens growth. *Vadose Zone J.* **12**.

PEPPIN, S. S. L., WETTLAUFER, J. S. & WORSTER, M. G. 2008*b* Experimental verification of morphological instability in freezing aqueous colloidal suspensions. *Phys. Rev. Lett.* **100** (23), 238301.

RAPATZ, G., MENZ, L. J. & LUYET, B. J. 1966 Anatomy of the freezing process in biological materials. In *Cryobiology* (ed. H. T. Meryman). Academic.

REMPEL, A. W. 2007 Formation of ice lenses and frost heave. *J. Geophys. Res. Earth Surf.* **112**, F02S21.

REMPEL, A. W. 2012 Hydromechanical processes in freezing soils. *Vadose Zone J.* **11**.

REMPEL, A. W., WETTLAUFER, J. S. & WORSTER, M. G. 2001 Interfacial premelting and the thermomolecular force: thermodynamic buoyancy. *Phys. Rev. Lett.* **87** (8), 088501.

REMPEL, A. W., WETTLAUFER, J. S. & WORSTER, M. G. 2004 Premelting dynamics in a continuum model of frost heave. *J. Fluid Mech.* **498**, 227–244.

STYLE, R. W. & PEPPIN, S. S. L. 2012 The kinetics of ice-lens growth in porous media. *J. Fluid Mech.* **692**, 482–498.

STYLE, R. W., PEPPIN, S. S. L., COCKS, A. C. F. & WETTLAUFER, J. S. 2011 Ice-lens formation and geometrical supercooling in soils and other colloidal materials. *Phys. Rev.* E **84** (4), 041402.

TABER, S. 1929 Frost heaving. *J. Geol.* **37**, 428–461.

TABER, S. 1930 The mechanics of frost heaving. *J. Geol.* **38**, 303–317.

https://doi.org/10.1017/jfm.2014.500 Published online by Cambridge University Press

TSAPIS, N., DUFRESNE, E. R., SINHA, S. S., RIERA, C. S., HUTCHINSON, J. W., MAHADEVAN, L. & WEITZ, D. A. 2005 Onset of buckling in drying droplets of colloidal suspensions. *Phys. Rev. Lett.* **94** (1), 018302.

VELEZ-RUIZ, J. F. & RAHMAN, M. S. 2007 *Handbook of Food Preservation*, chap. 26. CRC Press.

WATANABE, K. 2002 Relationship between growth rate and supercooling in the formation of ice lenses in a glass powder. *J. Cryst. Growth* **237**, 2194–2198.

WATANABE, K. & MIZOGUCHI, M. 2000 Ice configuration near a growing ice lens in a freezing porous medium consisting of micro glass particles. *J. Cryst. Growth* **213** (1), 135–140.

WETTLAUFER, J. S. & WORSTER, M. G. 2006 Premelting dynamics. *Annu. Rev. Fluid Mech.* **38**, 427–452.

ZHANG, H., HUSSAIN, I., BRUST, M., BUTLER, M. F., RANNARD, S. P. & COOPER, A. I. 2005 Aligned two-and three-dimensional structures by directional freezing of polymers and nanoparticles. *Nat. Mater.* **4** (10), 787–793.

https://doi.org/10.1017/jfm.2014.500 Published online by Cambridge University Press